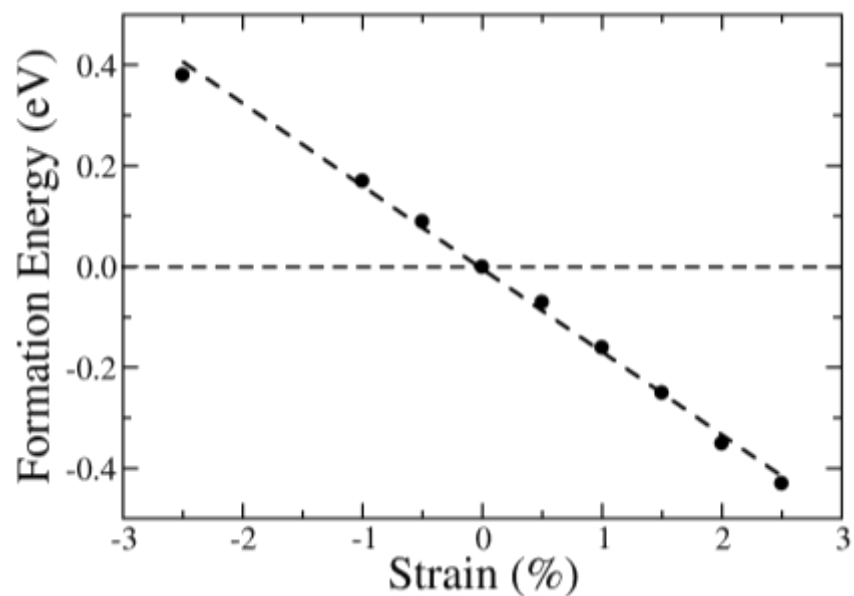
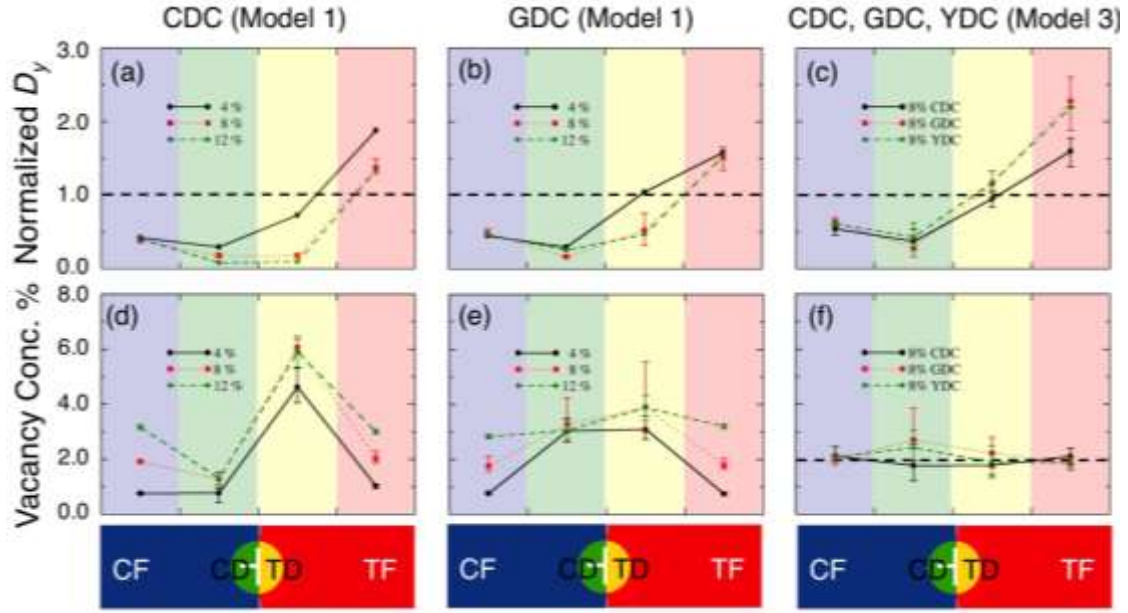


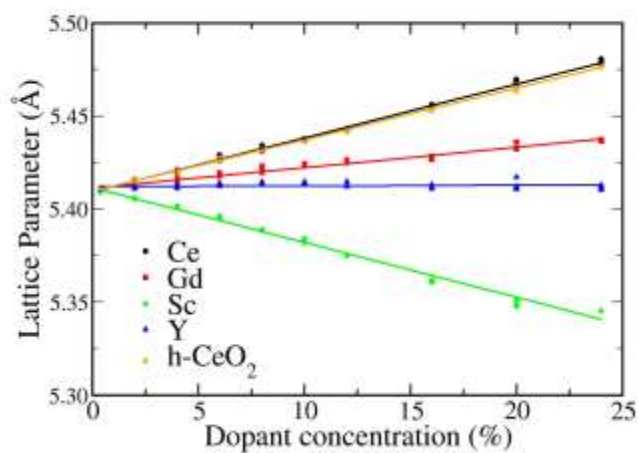
**Supplementary Figure 1 | The equilibrated distribution of trivalent cations in (a) reduced ceria (CDC) (b) gadolinia-doped ceria (GDC), with an average doping concentration (i) 4% (ii) 8% (iii) 12 % at 1300 °C, with the dislocation located at the center as shown in the schematic on the left for each row.**



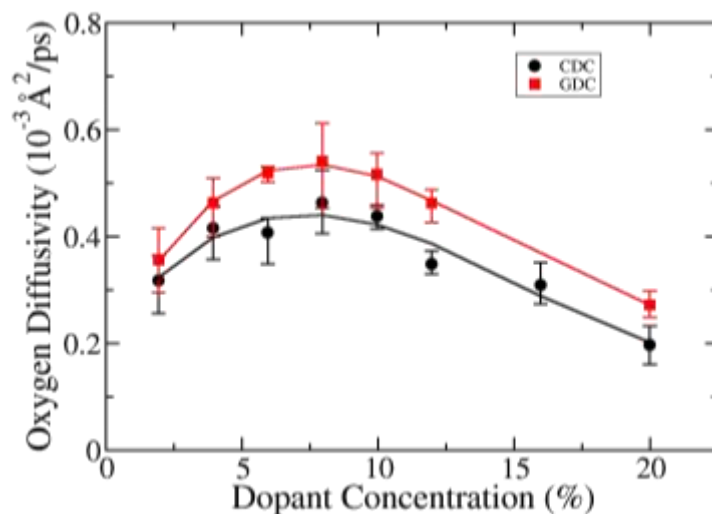
**Supplementary Figure 2 | The formation energy of oxygen vacancy in uniaxially strained bulk, dislocation-free ceria, plotted relative to the unstrained state.** When the bulk material is uniaxially strained along  $\langle 110 \rangle$  direction, the formation energy of oxygen vacancy decreases with the increasing strain. The positive strain represents tensile strain and the negative represents compressive strain. The oxygen formation energy in unstrained bulk material is chosen as the reference, marked as dashed line in the figure.



**Supplementary Figure 3 | Local oxide ion diffusivity along the dislocation,  $D_y$ , and local oxygen vacancy concentration, near and far from the dislocation at 900 °C: (a, d) for Model 1) of 4, 8 and 12 % CDC with equilibrated dopant cation distribution, (b, e) for Model 1) of 4, 8 and 12 % GDC with equilibrated dopant cation distribution, (c, f) for Model 3) of 8% CDC, 8% GDC and 8% YDC with random distribution of dopant cations. The geometry of the four regions for each of the three models is shown in the schematic plot below each column, and color-coded in the online version (yellow for the tensile dislocation region (TD) and green for the compressive dislocation region (CD), red for the uniaxial tensile region far from dislocation (TF), blue for uniaxial compressive region far from dislocation (CF)).**

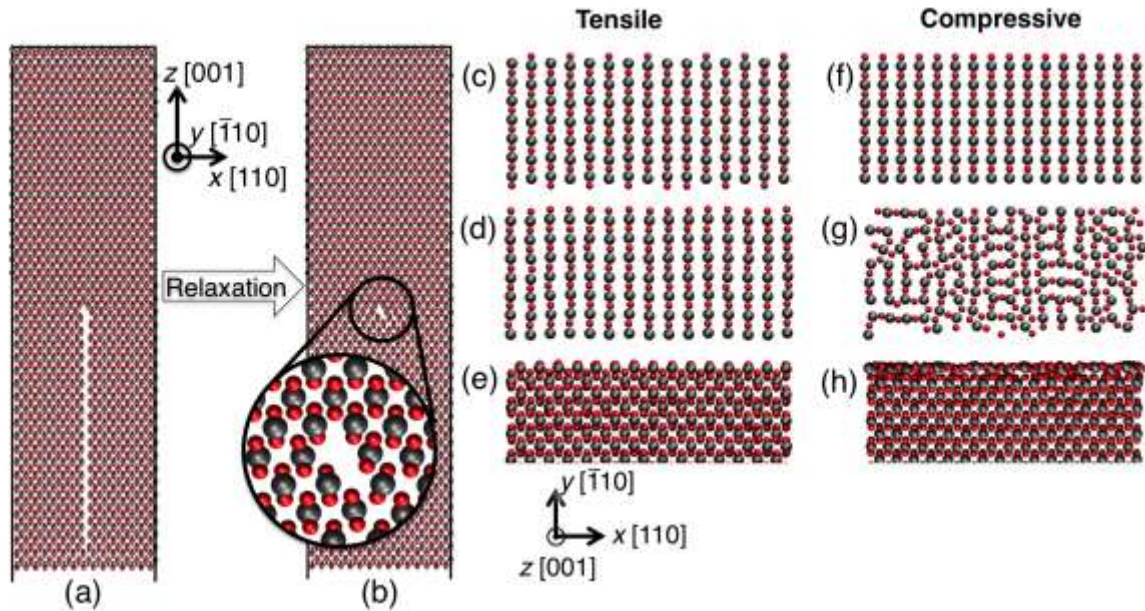


**Supplementary Figure 4 | The lattice parameter of CDC, GDC, SDC, YDC and h-CeO<sub>2-δ</sub> as a function of dopant concentration.**

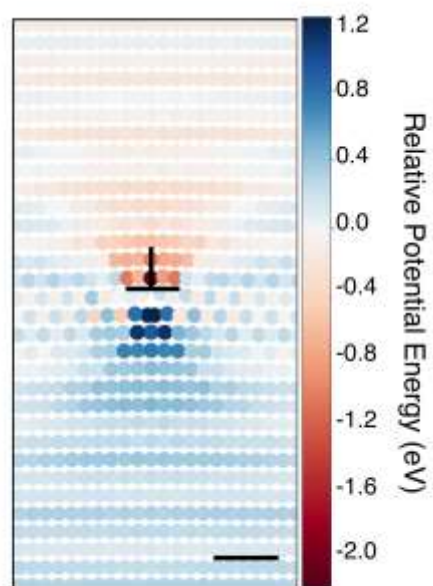


**Supplementary Figure 5 | Dependence of oxygen diffusivity on the concentration of trivalent cations.** The computed diffusivity of oxygen in CDC and GDC at 900 °C are shown by the black spheres and red squares, respectively. The lines are drawn to guide the eye. A smaller bulk ceria model made of 7776 atoms, without a dislocation, is modeled to calculate the oxygen diffusivity. **The dopant cations and oxygen vacancies are introduced randomly and optimized by the conjugate gradient algorithm at 0 K, followed by simulations of 100 ps in NPT and 100 ps NVT ensemble at 900°C.** The diffusivity is calculated by fitting the mean square displacement in a 1 ns long NVT simulation. Each data point is an average of three independent simulations. The error bar corresponds to the maximum and minimum diffusivity calculated among several simulations.

\* The diffusivity shown here is a three-dimensional diffusivity  $D_{3d} = \langle s^2 \rangle / 6t$ . The corresponding one-dimensional diffusivity used to normalized the diffusivity along dislocation is calculated by  $D_y = \langle s_y^2 \rangle / 2t$ .

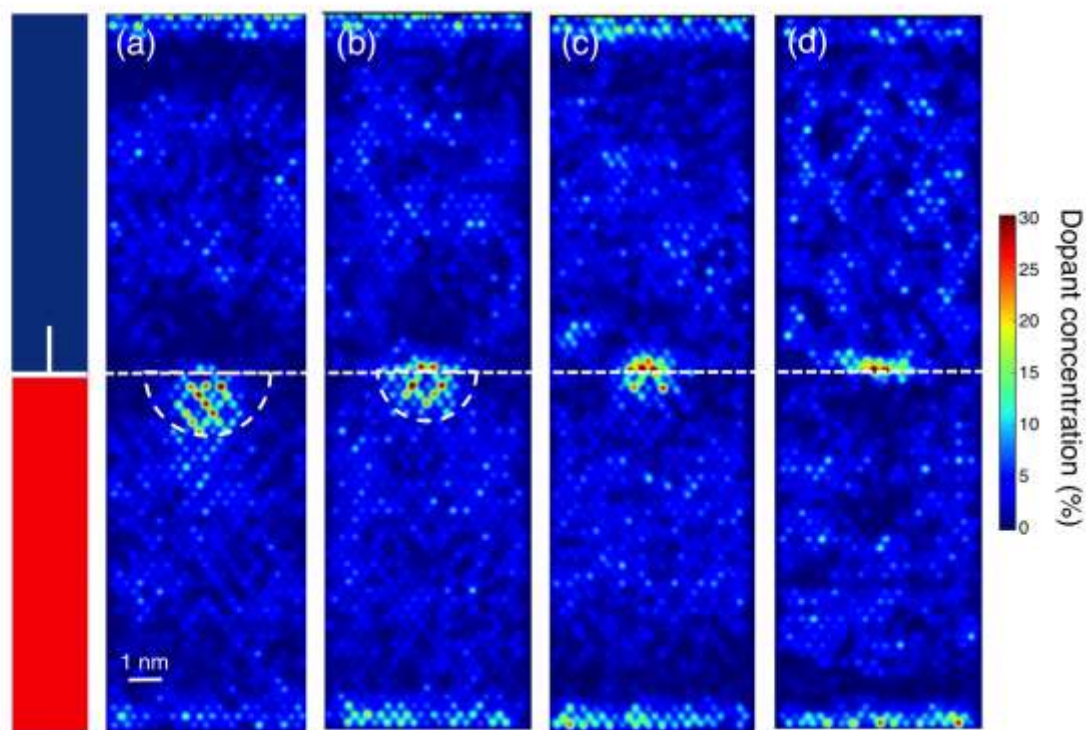


**Supplementary Figure 6 | Structural relaxation of the dislocation core structure and of the {100} surfaces. (a)** The  $\frac{1}{2} \langle 110 \rangle \{100\}$  edge dislocation is introduced to the slab with {100} surfaces, by deletion of half a lattice plane. **(b)** Meta-stable dislocation core structure in stoichiometric ceria gained by CG structure optimization of **(a)**. **(c, f)** Top view along  $[001]$  direction of {100} surfaces after CG optimization. Top view of the relaxed {100} surfaces along  $[001]$  direction in **(d, g)** and side view along  $\langle 110 \rangle$  direction in **(e, h)**, after 100 ps of MD simulation at 1000 °C followed by a constant pressure CG optimization. Both surfaces are strained along  $[\bar{1}10]$  direction by 2.6% tensile strain (as in **c-e**) and by 2.5% compressive strain (as in **f-h**).



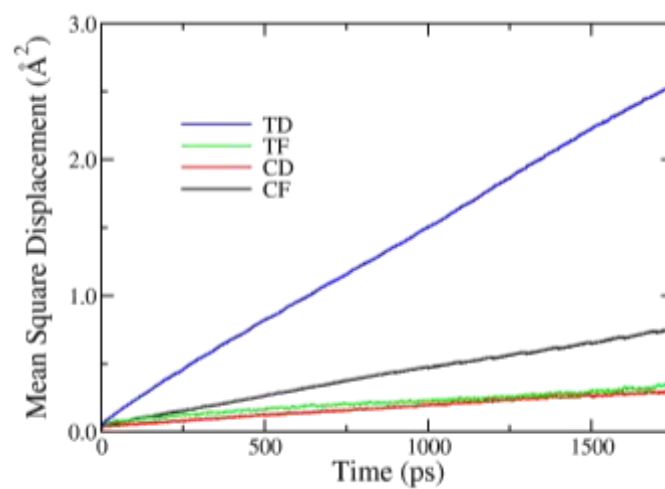
**Supplementary Figure 7 | Electrostatic potential energy of oxygen around the dislocation in a stoichiometric ceria model.** Electrostatic potential energy of each oxygen site is calculated as  $|E_O|$ . The potential energy of each oxygen ion in a slab of ceria, 26.72 eV, is chosen as the reference point. This value is different from an oxygen potential energy in a bulk ceria due to the summation method of long-range coulombic interaction in a non-periodic system.





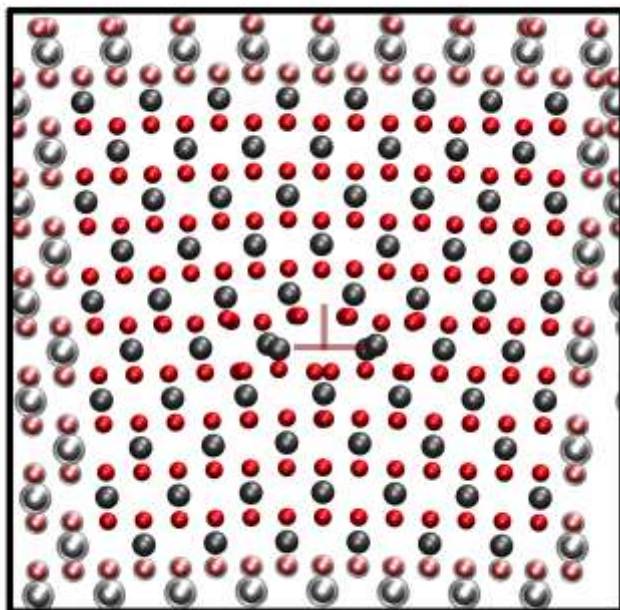
**Supplementary Figure 8 | The surface segregation of trivalent cations in (a) 8% CDC, (b) 8% GDC, (c) 8% yttria-doped ceria (YDC) and (d) 8% Scandia-doped ceria (SDC)**



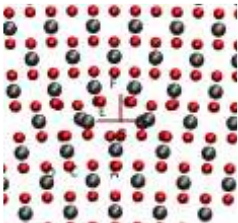








**Supplementary Figure 9 | The MSD versus time calculated at different regions for 8% CDC with equilibrated distribution of trivalent dopants at 900 °C.** The abbreviations in the legend are the same as in Supplementary Fig.

3.



**Supplementary Figure 10 | Oxygen reduction and electron localization around dislocations by DFT+U calculation.** An  $\frac{1}{2} \langle 110 \rangle \{100\}$  edge dislocation in ceria located in the center of the DFT simulation model. The red spheres represent oxygen ions and the gray spheres represent cerium ions. The atoms with a transparent shell are fixed during the structural relaxation.

Site	Relative formation energy (eV)	Position of oxygen vacancy	Site	Relative formation energy (eV)	Position of oxygen vacancy
A	0*				
B	0.10				
C	0.19				
D	0.53				
E	0.70				
F	1.40				
G	0.19		H	0.74	
I	0.54		J	0.69	
K	0.68		L	1.01	

**Supplementary Table 1 | Relative oxygen vacancy formation energy at different sites around the edge dislocation.** The schematic shows the position of oxygen vacancy at sites from A to J. For G-J, the black cube represents the oxygen vacancy position, and the solid blue sphere represents the two polarons that formed to compensate the charge of this oxygen vacancy, while all the other lattice atoms are shaded (hidden) through a transparent layer.

\* The formation energy in A is chosen as a reference.

	A (eV)	$\rho$ ( $\text{\AA}$ )	C (eV $\text{\AA}^{-6}$ )
$\text{O}^{2-}-\text{O}^{2-}$	9547.96	0.2192	32.0
$\text{Ce}^{4+}-\text{O}^{2-}$	1809.8	0.3547	20.40
$\text{Ce}^{3+}-\text{O}^{2-}$	2010.18	0.3449	23.11
$\text{La}^{3+}-\text{O}^{2-}$	2088.79	0.3460	23.25
$\text{Gd}^{3+}-\text{O}^{2-}$	1885.75	0.3399	20.34
$\text{Sc}^{3+}-\text{O}^{2-}$	1575.85	0.3211	0
$\text{Y}^{3+}-\text{O}^{2-}$	1766.40	0.33849	19.43

**Supplementary Table 2 | Parameterization of short range Buckingham potential in the rigid ion model**

$\alpha_c$	h-CeO <sub>2-<math>\delta</math></sub>	Ce <sup>3+</sup>	Gd <sup>3+</sup>	Y <sup>3+</sup>	Sc <sup>3+</sup>
Rigid Ion	0.0512	0.0533	0.0203	0.0006	-0.0545
Literature <sup>8</sup>		0.055-0.07	0.012-0.016	-0.0046	

**Supplementary Table 3 | Chemical expansion coefficient of reduced/doped ceria.**

## Supplementary Methods

**Classical interatomic potentials for reduced/doped ceria.** A rigid ion model is chosen to simulate the dislocation in structural relaxation, molecular dynamics (MD), and hybrid simulation combining MD and Monte Carlo (MCMD). The rigid ion model consists of a long-range electrostatic interaction between the nucleus and a short-range Buckingham potential

$$V_{\text{buckingham}}(r_{ij}) = Ae^{-r_{ij}/r} - C/r_{ij}^6 \quad (1)$$

Therefore, the total energy can be written as

$$E = \sum_{i < j}^N Ae^{-r_{ij}/r} - C/r_{ij}^6 + \frac{z_i z_j e^2}{r_{ij}}. \quad (2)$$

Previous studies showed that they are adequate to model the point-defect-dislocation interaction<sup>1,2</sup>. The Buckingham potential used in this work is parameterized by Minervini et al<sup>3</sup>, as listed in Supplementary Table 2. This potential can describe the lattice parameter, elastic constants, thermal expansion coefficient, heat capacity and formation energies of point defects<sup>4</sup>, and was validated by extensive comparison with experimental data. Recently, the potential was also successfully applied in studies of tilt grain boundaries<sup>5</sup> and surface segregation<sup>6</sup>.

For the hypothetical ceria model, h-CeO<sub>2-δ</sub>, a mean field potential is applied to the cation-anion interaction as shown below.

$$E(\text{Ce}^{(4-2\delta)+} \text{-O}^{2-}) = (1 - 2\delta) \times E_{\text{Ce}^{4+} \text{-O}^{2-}}^{\text{B}} + 2\delta \times E_{\text{Ce}^{3+} \text{-O}^{2-}}^{\text{B}} + \frac{(-2) \times (4 - 2\delta) e^2}{r_{ij}}$$

$$E_{\text{Ce}^{V+} \text{-O}^{2-}}^{\text{B}} = A_{\text{Ce}^{V+} \text{-O}^{2-}} \times \exp\left(-\frac{r_{ij}}{r_{\text{Ce}^{V+} \text{-O}^{2-}}}\right) + \frac{C_{\text{Ce}^{V+} \text{-O}^{2-}}}{r_{ij}^6}, \quad V = 3 \text{ or } 4$$

The valence of cerium cation is assigned to be (4-2δ) in order to compensate the charged induced by oxygen vacancies introduced. For example, δ=0.04 for 2% nominal concentration of vacancy and the cation valence is 3.92.

This rigid ion model is able to reproduce the lattice parameters for reduced ceria, GDC, YDC and SDC, where the lattice parameter of reduced/doped ceria depends on the trivalent cation concentration  $x$  in M<sub>x</sub>Ce<sub>1-x</sub>O<sub>2</sub>. A bulk ceria model with a size of 60.4 × 60.4 × 60.4 nm<sup>3</sup> and 20736 atoms is employed to model the variation of lattice parameter with composition. Four types of trivalent cations with a concentration ranging from 0.4% to 24%, as well as the hypothetical ceria model, h-CeO<sub>2-δ</sub>, are studied. Each data point in Supplementary Fig. 4 is an average over 4 simulations with different initial atomic configurations with randomly distributed dopant cations and oxygen vacancies, which are optimized by conjugate gradient algorithm at 0 K and zero pressure. The chemical expansion  $\epsilon_c$  is calculated by  $\epsilon_c = \frac{a - a_0}{a_0}$  and the chemical expansion coefficient  $\alpha_c = \epsilon_c/x$  can be then fitted, as shown in

Supplementary Fig. 4. The comparison of the rigid ion model used in this paper and literature is also listed in Supplementary Table 3.

Supplementary Fig. 5 shows the non-linear dependence of the oxygen diffusivity on the dopant concentration in the bulk CDC and GDC. As the dopant concentration increases, the oxygen diffusivity is enhanced until the dopant concentration reaches 8%. After reaching the maximum oxygen diffusivity, the diffusivity drops at higher dopant concentrations. The maximum diffusivity (at 8% dopant concentration) is  $0.458 \times 10^{-3} \text{Å}^2/\text{ps}$  and  $0.501 \times 10^{-3} \text{Å}^2/\text{ps}$  in CDC and GDC, respectively. This trend is well consistent with previous literature<sup>7</sup>. In the real reduced or doped ceria, the optimum concentration may be slightly different. However, the conclusions in the main text hold true as long as this non-linear dependence of diffusivity on concentration is present.

**The mean square displacement (MSD) calculation along the dislocation.** The MSDs in the paper and the supplemental material are calculated by Molecular Dynamics implemented in LAMMPS. The time step is 0.5-1 fs, chosen as small as it is to conserve the energy of the simulated system. Before the MSD calculation, the system is relaxed for 200 ps in the isothermal-isobaric (NPT) ensemble and another 200 ps in the canonical (NVT) ensemble with Nose–Hoover thermostat and barostat relaxation times of 0.5 ps. The thermostat and barostat parameters are large enough to capture the dynamic of oxygen migration. Supplementary Fig. 9 shows the local MSD of four different regions in 8% CDC at 900 °C. The statistics is improved by using multiple time origins. Each MSD point is averaged over 20 time origins.

The local diffusivity is calculated by the MSD of oxygen in 3-5 samples for each model. The error bounds for the diffusivity and the vacancy concentration are derived from the maximum and minimum values among these samples. The four regions TD, TF, CD and CF (see also Fig. 1) are defined by the following geometric criteria: TF and CF are 3-nm-thick slabs, whose center is 4.5 nm away from the glide plane, while the TD and CD are semi-cylindrical regions centered at the dislocation core with 1.5 nm radius. The four regions (TD, TF, CD and CF) have approximately 400, 2300, 500, 2400 oxygen atoms. The CD, TD regions have relatively fewer oxygen atoms, which results in larger error bars, as shown in Supplementary Fig. 3(d-f).

**Density functional theory calculation of defects around the dislocation.** The Density Functional Theory calculations reported in this paper were performed with the VASP code, within the Projector Augmented Wave (PAW) method. We used the Generalized Gradient Approximation (GGA) with the Perdew-Wang 91 (PW91) exchange-correlation functional and an energy cutoff of 400 eV. A Hubbard (+U) correction, with  $U = 5$  eV on the cerium ions, was added to properly model the localized character of the 4f electrons. All the calculations were carried out using the Brillouin zone sampled with a  $(1 \times 2 \times 1)$  Monkhorst-Pack mesh k-points grid.

The model of dislocation is constructed by removal of half lattice plane and displacing the atoms around based on elastic theory, which is implemented in the ATOMSK code developed by Dr. Pierre Hirel<sup>10</sup>. As shown in Supplementary Fig. 10a, the system contains 612 atoms with the dislocation at the center. The system has periodic boundaries over all three directions while the atoms at  $x$  and  $y$  boundaries of the system are fixed during the whole relaxation (shown as spheres with transparent shell in Supplementary Fig. 10a).

The oxygen vacancy formation energy is calculated at different sites around the dislocation. The spin density in Supplementary Fig. 10b shows that the two electrons left by the removal of oxygen are localized on two cerium ions, forming two  $\text{Ce}^{3+}$ , even when the vacancy site is right at the dislocation core. Therefore, we confirm that the charge compensation mechanism does not change at the dislocation core.

The vacancy formation energy is reported in Supplementary Table 1. For the vacancy site at A-F, the system is relaxed by CG optimization right after the removal of oxygen. For the position G-J, the arrangement of two  $\text{Ce}^{3+}$  ions is controlled by using a  $\text{Ce}^{3+}$  pseudo-potential. This pseudo-potential forces one 4f electron to a core electron and maintains the valence of ion to be 3+. After structural optimization, the system is relaxed again with a GGA+U approach. We find that the polarons do not move during this second relaxation. Cases G-J shows that polarons prefer to stay at the tensile zone around the dislocation than being at the nearest neighbor site of the oxygen vacancies. This indicates that in reduced ceria, the elastic energy minimization is the dominant factor of  $\text{Ce}^{3+}$  segregation.

## Supplementary References

1. Puls, M. P. Vacancy-dislocation interaction energies in MgO A re-analysis. *Philos. Mag. A* **47**, 497–513 (1983).

2. Puls, M. P., Woo, C. H. & Norgett, M. J. Shell-model calculations of interaction energies between point defects and dislocations in ionic crystals. *Philos. Mag.* **36**, 1457–1472 (1977).
3. Minervini, L., Zacate, M. O. & Grimes, R. W. Defect cluster formation in  $M_2O_3$ -doped  $CeO_2$ . *Solid State Ion.* **116**, 339–349 (1999).
4. Xu, H. et al. A critical assessment of interatomic potentials for ceria with application to its elastic properties. *Solid State Ion.* **181**, 551–556 (2010).
5. Lee, H. B., Prinz, F. B. & Cai, W. Atomistic simulations of grain boundary segregation in nanocrystalline yttria-stabilized zirconia and gadolinia-doped ceria solid oxide electrolytes. *Acta Mater.* **61**, 3872–3887 (2013).
6. Lee, H. B., Prinz, F. B. & Cai, W. Atomistic simulations of surface segregation of defects in solid oxide electrolytes. *Acta Mater.* **58**, 2197–2206 (2010).
7. Kilner, J. A. Fast oxygen transport in acceptor doped oxides. *Solid State Ion.* **129**, 13–23 (2000).
8. Marrocchelli, D., Bishop, S. R., Tuller, H. L. & Yildiz, B. Understanding Chemical Expansion in Non-Stoichiometric Oxides: Ceria and Zirconia Case Studies. *Adv. Funct. Mater.* **22**, 1958–1965 (2012).
9. Nolan, M., Grigoleit, S., Sayle, D. C., Parker, S. C. & Watson, G. W. Density functional theory studies of the structure and electronic structure of pure and defective low index surfaces of ceria. *Surf. Sci.* **576**, 217–229 (2005).
10. Hirel, P., Mrovec, M. & Elsässer, C. Atomistic simulation study of  $\langle 110 \rangle$  dislocations in strontium titanate. *Acta Mater.* **60**, 329–338 (2012).